Dalton Transactions

ROYAL SOCIETY OF CHEMISTRY

PAPER

View Article Online
View Journal | View Issue

Cite this: *Dalton Trans.*, 2025, **54**, 4577

Transforming delayed fluorescence into blue-shifted phosphorescence in aminoboranes *via* oxygen-to-sulfur substitution on the donor amine†

Akkarakkaran Thayyil Muhammed Munthasir, * Satyam Jena and Pakkirisamy Thilagar*

Received 15th November 2024,
Accepted 20th January 2025

DOI: 10.1039/d4dt03200d

rsc.li/dalton

Thermally activated delayed fluorescence (TADF) and room-temperature phosphorescence (RTP) materials are found in diverse applications, from optoelectronic devices to time-gated bioimaging. Recently, aminoboranes with donor–acceptor structures have been identified as promising candidates due to their inherent capacity to harvest the triplet excitons by their unique orbital configurations (El Sayed rule). This work reports the delayed luminescence behaviors of two aminoboranes, **BNO** and **BNS**, featuring phenoxazine (PXZ) or phenothiazine (PTZ) donors coupled with a dixylylborane acceptor. **BNO** exhibits efficient TADF emission in aggregates, thin films, and solid states. In contrast, **BNS** shows delayed fluorescence (DF) in aggregate states and RTP in solid and thin-film states. Notably, **BNS** shows a rare blue-shifted phosphorescence relative to its prompt fluorescence, which has not been reported for aminoboranes. Photoluminescence studies and computational calculations reveal that ISC and rISC processes in these systems involve higher triplet states. The unprecedented blue-shifted phosphorescence in **BNS** is attributed to perturbations in energy levels, which are driven by unique quasi-axial and quasi-equatorial conformations and the stronger spin–orbit coupling of heavier S over O.

Introduction

Luminescence efficiency is a critical parameter that determines the viability of a material for practical applications.[1–6] Contemporary research has primarily focused on developing innovative designs and strategies to achieve energy-efficient systems. Conventional fluorescence relies solely on singlet-state emission, prompting extensive research into harnessing the dark triplet state to enhance the luminescence efficiency.[7–10] To date, several innovative approaches have been reported, including phosphorescence (PH),[11–16] delayed fluorescence (DF),[17–22] processes such as triplet–triplet annihilation (TTA),[23–26] thermally activated delayed fluorescence (TADF),[27–32] and, most recently, hybridized local charge transfer (HLCT),[33–36] offering new avenues for improved performance. Among these, phosphorescence and TADF materials are found to be prominent and have found application in various fields such as organic light-emitting diodes (OLEDs),[31,37–40] bioimaging and biosensing,[41–43] security and anti-counterfeiting,[44–46] sensing,[47–49] solar cells, energy harvesting, *etc.*[50–52]

Phosphorescence involves two consecutive spin-forbidden processes, intersystem crossing (ISC) ($S_1 \rightarrow T_n$) followed by radiative decay from $T_n \rightarrow S_0$.[11–16] The weak spin–orbit coupling (SOC) in organic molecules limits the development of purely organic phosphorescence materials. However, this hurdle has been overcome by incorporating heteroatoms (N, P, O, S, *etc.*), and heavy atoms (Br, Cl, Se *etc.*), which enhances ISC rates and triplet state populations, consistent with El-Sayed's rule and the heavy atom effect.[53–57] Meanwhile, TADF is an unimolecular process that utilizes reverse intersystem crossing (rISC) to convert triplet-state populations to singlet states, facilitated by thermal energy. The rate of this up-conversion process is inversely correlated with the singlet to triplet energy gap, ΔE_{ST}, governed by the equation $k_{rISC} = Ae^{-\frac{\Delta E_{ST}}{k_B T}}$, highlighting the importance of minimizing ΔE_{ST} for efficient TADF processes.[27–32,58,59] This can be achieved by designing twisted donor–acceptor (D–A) systems having minimal electronic overlap between the highest occupied molecular orbital (HOMO) and the lowest unoccupied molecular orbital (LUMO).[27–32]

Aminoboranes are a new class of systems recently added to the family of delayed luminescent materials. Their unique

---

Department of Inorganic and Physical Chemistry, Indian Institute of Science, Bangalore, 560012, India. E-mail: thilagar@iisc.ac.in

† Electronic supplementary information (ESI) available. CCDC 2402292. For ESI and crystallographic data in CIF or other electronic format see DOI: **https://doi.org/10.1039/d4dt03200d**

molecular architecture and access to electronic states of different symmetry (π–π* and n–π*/CT and LE) between singlet and triplet leads to enhanced SOC, which enables efficient ISC and rISC for delayed emission.[38–40,60–63] Moreover, aminoboranes are well known for their distinctive stimuli-responsive properties.[64–66] Thus, aminoboranes find applications in various fields. For instance, in 2017, Yun Chi and co-workers reported the first TADF from an aminoborane system, using an acridine-decorated aminoborane to develop a green OLED.[39] In 2018, Chen *et al*. developed boryl-substituted phenoxazine that exhibits efficient TADF capable of producing highly efficient orange OLEDs.[38] In 2020 Yun Chi's group again developed an OLED with blue light emission from a methoxy-substituted carbazole-based aminoborane.[40] He and co-workers demonstrated ultralong organic phosphorescence (UOP) from a carbazole-based aminoborane that same year.[61] Our group has also been active in aminoborane research for the past decade. In 2017, Neena *et al.* showed aggregation-induced emission AIE and triboluminescence properties in diphenylamine and phenothiazine-decorated aminoboranes, respectively.[64,67] In 2018, we explored a vinyl-pyridyl-decorated aminoborane for barrier-free DF.[63] Recently, in 2023, we reported intense blue circularly polarized luminescence from a chiral aminoborane, and in the same year, we demonstrated persistent RTP with a 470 ms lifetime from molecularly dispersed aminoboranes.[62,66]

As part of our ongoing program, we intend to investigate the influence of the heteroatoms and the conformational dynamics of the nonplanar donor attached to an aryl borane acceptor on its singlet/triplet state energetics and delayed luminescence behavior. For this study, we have chosen the phenoxazine (PXZ) and phenothiazine (PTZ)-decorated aminoboranes **BNO** and **BNS**, respectively, as the lighter atom, O in phenoxazine, and heavier atom, S in phenothiazine, may impart different amounts of spin–orbit coupling in these molecules and endow them with unique delayed luminescence characterstics (Fig. 1). Furthermore, the nonplanar heterocycles PXZ and PTZ in these molecules can exhibit quasi-equatorial and quasi-axial conformational dynamics that are susceptible to the microenvironment, by this means modifying the energetics of the singlet and triplet states and, therefore, their emission properties.[68–75] In light of these factors, we present a comprehensive photophysical and theoretical analysis of **BNO** and **BNS**. The results reveal that **BNO** exhibits efficient TADF emission in both dispersed and condensed states, while **BNS** demonstrates delayed fluorescence in aggregates and rare, blue-shifted phosphorescence in the solid state and as polymer-doped film. Our detailed study concludes that the heavy atom effect of sulfur over oxygen, coupled with the pronounced flip-flop motion of PTZ, is responsible for the distinct delayed emission features in **BNS** over **BNO**. These intriguing findings are discussed in this manuscript.

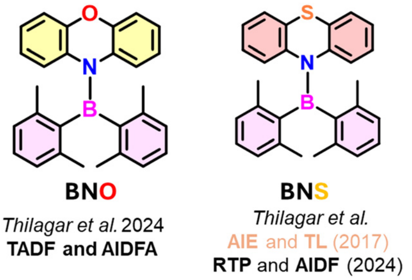

Fig. 1 Chemical structures of the aminoboranes under investigation.

Results and discussion

Synthesis and structural studies

Both **BNO** and **BNS** were synthesized following the literature procedures (Schemes 1 and S1, S2†).[38,64] The synthesis involves lithiation of phenoxazine or phenothiazine using *n*-butyllithium, followed by quenching of the lithiated intermediate with bis(2,6-dimethylphenyl)fluoroborane. Analytically pure **BNO** and **BNS** were obtained through column chromatography, which was followed by recrystallization. Both compounds were characterized using NMR spectroscopy (^{1}H, ^{13}C, ^{11}B) and high-resolution mass spectrometry (HRMS) (Fig. S1–S8†). The molecular structure of **BNO** was confirmed by single-crystal X-ray diffraction (SCXRD) analysis (Fig. 2 and Table S1†). ^{1}H NMR analysis indicated that **BNO** adopts $C2$ symmetry in $CDCl_3$, similar to its mesityl analog (**R1**)[38] and many reported aminoboranes.[38–40,61–67] The ^{11}B NMR resonance for **BNO** appears at 50.7 ppm, consistent with aminoborane systems exhibiting significant B–N π-bond character (Fig. S3†).[38–40,61–67] The characterization data for **BNS** exactly matched the literature report, so the molecular structure previously reported by Neena *et al.* was used for further structural comparisons.[64]

Pale yellow block-shaped crystals of **BNO** suitable for single-crystal X-ray diffraction studies were obtained by slow evaporation of a DCM : hexane solution (3 : 1 ratio). **BNO** crystallizes in the triclinic crystal system with the $P\bar{1}$ space group (Fig. 2a and Table S1†). Similar to its mesityl analog **R1** (Fig. S13†), the B(1) center in **BNO** adopts trigonal planar geometry with a B–N bond length of 1.433 Å, comparable to that in **R1** (1.438 Å), **BNS** (1.455 Å) and other aminoboranes (Table S2†).[38–40] The dihedral angle between the C(28)N(1)C(C17) plane (PXZ) and the C(1)B(1)C(7) plane (boryl) is 29°, which is higher than the value noted for **R1** (25°) and **BNS** (22°), suggesting better in-plane arrangement of donor–acceptor moieties and greater electronic communication in **BNO** than in the other two com-

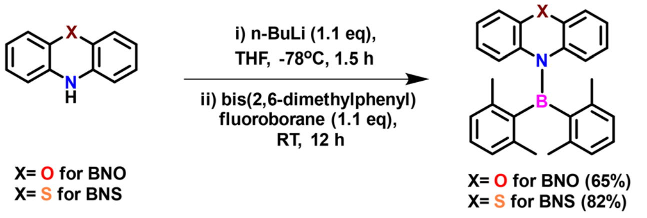

Scheme 1 Synthesis scheme for BNO and BNS.

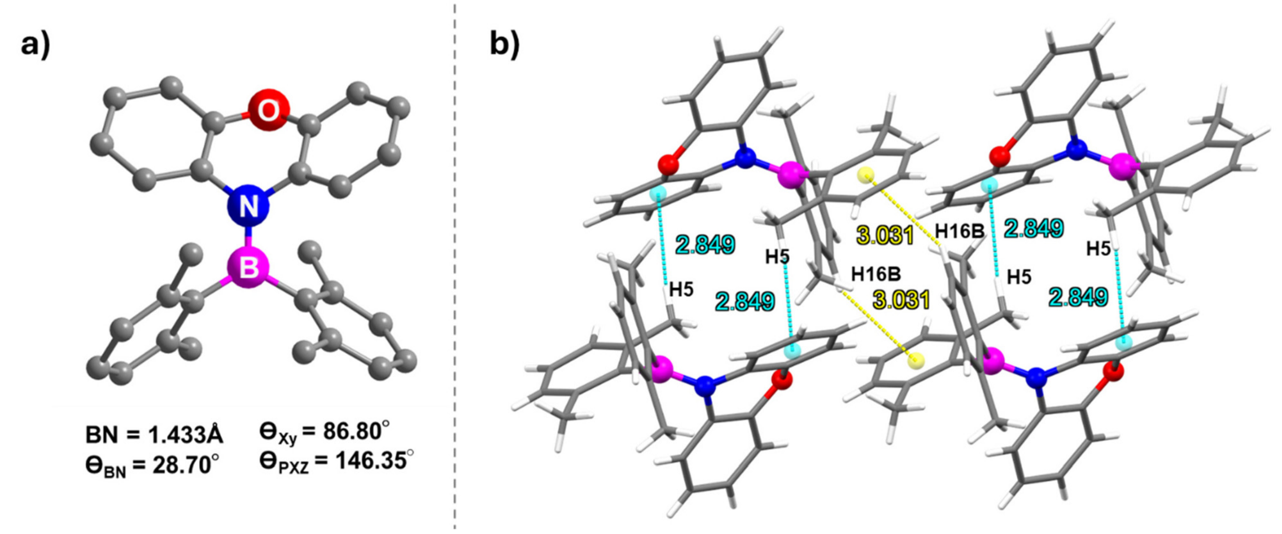

Fig. 2 (a) Molecular structure of **BNO**, and (b) supramolecular dimer chains of **BNO**. Cyan and yellow dashed lines represent the CH⋯π interactions. Atom colour code – carbon: grey, nitrogen: blue, oxygen: red, and hydrogen: off-white.

pounds (Fig. S9†).[38,64] The dihedral angle between the aryl groups on boron is larger in **BNO** (86.80°) than in **BNS** (82.73°), allowing more spatial accommodation for PXZ and resulting in a slightly shorter B–N bond (Fig. S10†). Additionally, the twist angle between the two benzene rings of PXZ in **BNO** is 146.35°, similar to that in **R1** (142.70°), indicating a saddle-like nonplanar geometry for PXZ (Fig. S11†). However, this twist angle is notably higher in the PTZ unit of **BNS** (134.08°), suggesting that PXZ connected to arylborane in **BNO** is more planar than PTZ in **BNS**. This planarity likely contributes to denser packing in **BNO** (ρ_{calcd} = 1.215 g cm^{-3}) than in **BNS** (ρ_{calcd} = 1.174 g cm^{-3}).

The intermolecular CH⋯π interaction (2.849 Å) between a C–H of a xylyl ring and the xylyl π-cloud of an adjacent molecule generates a supramolecular dimer (Fig. 2b). The neighboring dimers are stitched together by the CH⋯π interaction (3.031 Å) between the methyl proton (H16B) on the xylyl unit of one molecule and the π cloud of one of the benzo groups of phenoxazine on the adjacent dimer leading to the formation of the supramolecular 2D chain (Fig. S12†). In contrast, the more puckered nature of PTZ in **BNS** leads to a less dense packing arrangement, forming a "3D supramolecular structure with cylindrical columns of diameter 4.61 Å", as reported by Neena *et al.*[64] These structural and packing differences between **BNO** and **BNS** could have a significant impact on their optoelectronic properties.

Photophysical and theoretical studies

Solution state PL studies. Hexane solutions of **BNO** show a broad absorption band ranging from 240–380 nm with two distinct band maxima at 280 nm and 320 nm with no significant shift with the solvent polarity (Fig. 3a and c and Table S6†). The lower energy band in **BNO** is similar to the band observed in **R1**, which is attributed to the charge transfer band, though there is no significant change in the absorption maxima with change in solvent polarity (Fig. 3c).[38] On the other hand, the higher energy band at 280 nm in **BNO** is in line with that of **BNS**, suggesting this band could be due to the local transition in phenoxazine (π → π*) and aryl borane units (π → $P_\pi B$). As shown in Fig. 3a, the absorption features observed for **BNS** are similar to those of the previous report, where the lower energy bands are very week or absent (Fig. S15a, and Table S6†).[64]

To understand the absorption features of **BNO** in detail, we optimized the ground state geometry for **BNO**, and singlet vertical transitions were calculated using density functional theory (DFT) and time-dependent DFT (TD-DFT), respectively (Fig. 3b and S14, S15†). The bond parameters of the optimized geometry are closely matched with those of the crystal structure, validating the choice of level of theory (Table S3†). The HOMO is localized over the phenoxazine moiety, whereas the LUMO is localized all over the molecule with a significant contribution from boron. Similar features were observed in **BNS** also (Fig. 3b). Upon changing PTZ to PXZ (in **BNO**), the HOMO of the molecule is slightly destabilized, while the LUMO is stabilized, resulting in a reduction in the band gap (ΔE_g = 4.63 eV) compared to **BNS** (ΔE_g = 4.76 eV), with the same reflected in their respective absorption spectra (Fig. 3a and c).

The vertical transition calculation revealed that the lower energy absorption band at 320 nm for **BNO** results from the S_0 to S_1 transition involving the HOMO and LUMO (f = 0.1589) (Fig. S14†). As discussed above, the HOMO and LUMO are localized on different parts of the molecule suggesting the lowest energy HOMO → LUMO transition is an intramolecular charge transfer (ICT) from the donor amine to the acceptor boryl moieties. On the other hand, the higher energy band is a collection of S_0 to S_n (n = 2, 3 and 4) transitions involving electronic distribution within the PXZ ring or boryl units (Fig. S14 and Table S4†). A similar scenario is observed in the case of

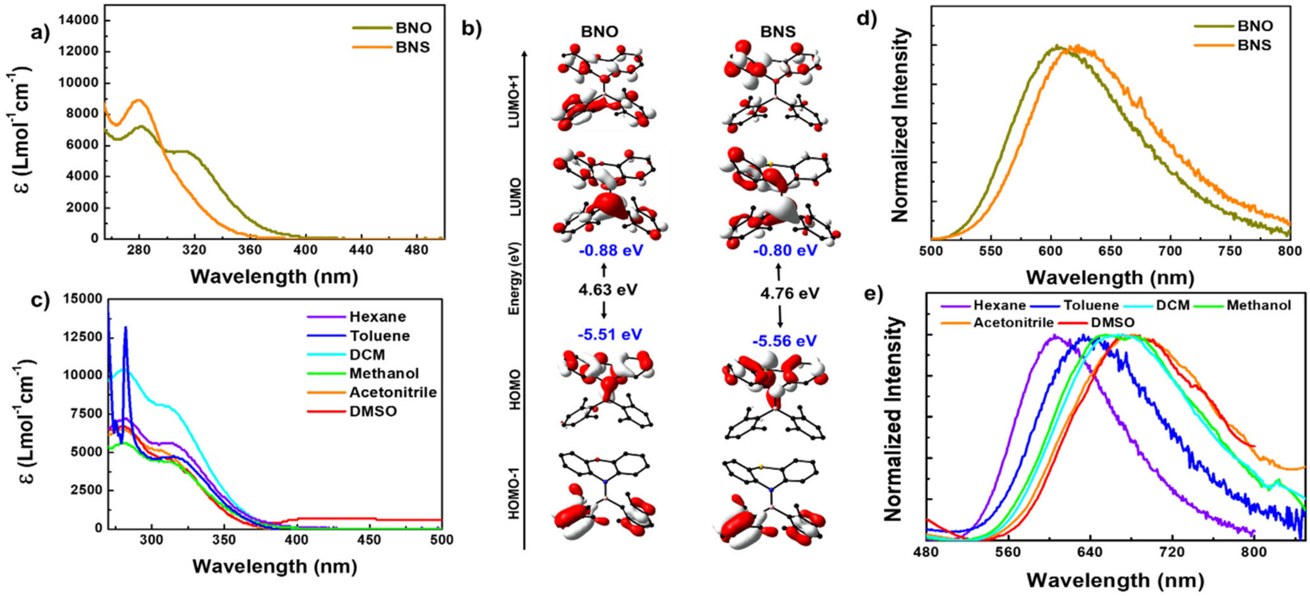

Fig. 3 (a) Absorption spectra of **BNO** and **BNS** in hexane (conc. 10^{-5} M). (b) Frontier molecular orbitals for **BNO** and **BNS** obtained from the optimized geometry using DFT [the B3LYP/6-31G(d) level of theory]. (c) Absorption spectra of **BNO** in different solvents (conc. 10^{-5} M). (d) Steady-state PL spectra for **BNO** and **BNS** in hexane and (e) steady-state PL spectra of **BNO** in different solvents (conc. 10^{-5} M) at λ_{ex} = 310 nm for **BNO** and 290 nm for **BNS** under ambient conditions.

BNS; however, the transition probability for S_0 to S_1 (303.04 nm, f = 0.0094) is quite low, resulting in a weak CT band (Fig. S15 and Table S5†).

The photoluminescence (PL) spectra of **BNO** in hexane display a broad emission band ranging from 500 to 800 nm with a peak maximum at 605 nm. This emission band is 15 nm blue-shifted compared to the PL of **BNS** (Fig. 3d). Upon increasing solvent polarity, the emission maximum is red-shifted with a drastic decrease in the PL intensity, which is typical of D–A systems (Fig. 3e and S17c†). Similar to **R1**, the **BNO** also shows a very large Stokes shift (15217 cm^{-1}) indicating that large structural reorganization occurred in the excited state.[38] The TD-DFT-optimized S_1 geometry indeed showed large structural variations; the nonplanar PXZ ring in S_0 became completely planar along with the BN bond elongation, supporting the large Stokes shift (Fig. S16 and Table S3†). The degree of ring planarization in **BNO** is slightly lower than that in its mesityl analog **R1**; consequently, **BNO** exhibits a smaller Stokes shift than **R1**. The phenothiazine ring in **BNS** also undergoes planarization (to a greater extent than that in **BNO**) resulting in a large Stokes shift (Fig. S16 and S18†).[38] Because of the large structural reorganization/flip-flop motion of the PXZ unit, **BNO** is weakly emissive in the dilute solution. Despite this weak emission, **BNO** shows a delayed fluorescence (DF) band, which overlaps smoothly with the fluorescence spectra, revealing the DF nature of the emission (Fig. S19a†). The lifetime measurement revealed that **BNO** exhibits both ns (13.60 ns) and μs (6.38 μs) for the same peak maximum further affirming the TADF characteristics (Fig. S19d and Table S7†). Under the oxygen environment, the PL intensity, lifetime, and photoluminescence quantum yield (PLQY) of **BNO** decreased considerably (Fig. S19 and Table S7†). No such DF is observed for **BNS** under similar conditions.

Furthermore, to understand the Lewis acidic nature of the boron center, these aminoboranes are titrated against pyridine/F^- and the binding events are monitored using absorption and PL spectrometers. The result shows that pyridine does not bind to the Lewis acid boron; however, F^- binds with these aminoboranes and causes significant spectral changes. Upon binding with fluoride (TBAF), the absorption bands show a bathochromic shift, while the PL bands exhibit a hypsochromic shift (Fig. S20 and S21 in the revised ESI†). These spectral changes can be attributed to the geometry changes at the boron center of trigonal planar to tetrahedral and the breaking of conjugation between the empty p orbital of boron and lone-pair electrons of nitrogen in the amine moiety. The calculated binding constants for **BNO** and **BNS** are 2.09×10^4 and 1.94×10^4, respectively. These values are significantly lower than the ones reported for triarylboranes elsewhere, indicating that the Lewis acidity of B is significantly reduced in aminoboranes due to the resonance bonding interactions between the empty p orbital of acceptor and lone-pair electrons of N in the donor moiety.[76–78]

Aggregate state PL studies. The primary reason for the weak emission of **BNO** and **BNS** in the dispersed state is attributed to the intramolecular motion in the excited state. In 2017, Neena *et al.* reported aggregation-induced emission enhancement (AIEE) in **BNS**, observing a remarkable 180-fold increase in emission in a THF–water mixture (f_w = 90%).[64] Compound **BNO** also showed AIEE; at lower water content (f_w < 40%), it exhibited weaker emission at 687 nm. At f_w = 40% to f_w = 70%, the PL intensity increased with a concomitant gradual hypsochromic shift from 687 nm to 535 nm. With a further increase in water fraction, a slight decrease in intensity and bathochromic shift (from 535 nm to 580 nm) was observed, followed by a sharp rise in the PL intensity at f_w = 90% (Fig. 4a and S22†).[79–81] These distinct emission features at f_w = 70% and 90% are attributed to the formation of different types of emissive aggregates with varying sizes and morphologies, as confirmed by TEM analysis (Fig. S24†).

We further analysed the delayed emission behaviour of **BNO** aggregates at f_w = 70% and f_w = 90%. As anticipated, the aggregates exhibited more efficient DF than the dilute solution (Fig. 4b–f and S23†). The prompt and delayed emission spectra overlapped smoothly, and both the lifetime and quantum yield increased significantly compared to the solution (Fig. 4b–f, S23 and Table S8†). The lifetime (prompt and delayed) and PLQY of aggregates at f_w = 70% (Φ_{Total} = 0.23) were found to be higher than those at f_w = 90% (Φ_{Total} = 0.18) and showed greater sensitivity to oxygen (Fig. S23, and Table S8†). This difference can be attributed to the greater crystallinity of the particles formed at f_w = 90% than at f_w = 70% (Fig. 4c–f, S24, and Table S8†). These results suggest that both singlet and triplet manifolds are affected by the size, morphology, and crystallinity of the aggregates formed at different water fractions (f_w).

Although the AIEE behavior of **BNS** was reported previously, its aggregate-state delayed luminescence features had not been explored.[64] To further substantiate the DF phenomena at the aggregate level, we conducted similar experiments on **BNS**. This compound exhibited significant emission enhancement with a blue shift (580 nm) in a water–DMSO mixture at f_w = 90%, consistent with observations reported elsewhere (Fig. S25a†). Time-gated spectra recorded for these aggregates revealed the DF nature of **BNS** with a smooth overlap of prompt and delayed spectra. **BNS** shows higher PLQY (0.32) than **BNO** (0.25), though with a DF lifetime value nearly half that of **BNO** (Fig. S25b–S25f and Table S9†). Detailed studies including lifetime and quantum yield and various radiative and non-radiative decay rates are given in Table 1 and S8–S10.† Furthermore, the aggregates formed from **BNS** are amorphous, hence, the molecules may not adopt a specific conformation such as quasi-axial or quasi-equatorial (Fig. S24†). In contrast, in solid or thin-film forms, the molecules exhibit high crystallinity and adopt a preferential conformation, which explains the observed differences in their emission properties. This is discussed in detail in the following section.

In short, **BNO** exhibits a weak fluorescence and DF in a molecularly dispersed solution due to active molecular motion, which increases non-radiative decay from the emissive state. However, at the aggregate state, both **BNS** and **BNO** demonstrate luminescence enhancement. Both **BNO** and **BNS** showed efficient delayed fluorescence in the aggregated state. Moreover, the PL features of **BNO** depend on the morphology and size of the aggregates. Though the phenomenon of aggregation-induced delayed fluorescence (AIDF) is well documented in the literature, such phenomena are rare in B–N systems, highlighting the significance of these findings.[82–86]

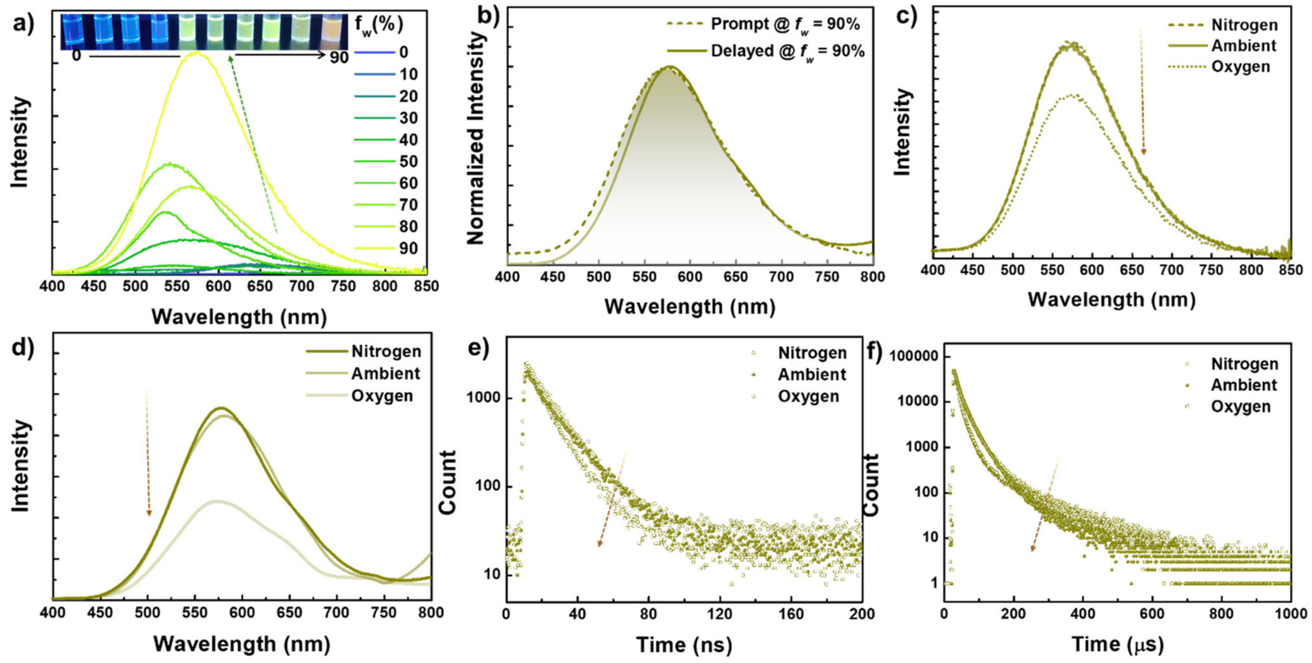

Fig. 4 (a) Steady-state PL spectra of **BNO** in DMSO with different fractions of water [f_w] at λ_{ex} = 310 nm. (b) Prompt and time-gated/delayed [20 μs delay] PL spectra for **BNO** in degassed DMSO–water mixture [f_w = 90%] at λ_{ex} = 310 nm. (c) Steady-state and (d) time-gated/delayed [20 μs delay] PL spectra for **BNO** in DMSO–water mixture [f_w = 90%] in a different environment at λ_{ex} = 310 nm. (e) Fluorescence and (f) delayed fluorescence decay for **BNO** in DMSO–water mixture [f_w = 90%] in a different environment at λ_{ex} = 310 nm and λ_{em} = 580 nm.

Table 1 Prompt fluorescence (PF) and delayed fluorescence (DF) lifetimes, and total photoluminescence quantum yield for **BNO** and **BNS** in degassed hexane and DMSO–water mixtures (f_w = 70% and f_w = 90%)

	λ_{ex} (nm)	λ_{em} (nm)	Fluorescence τ_1 (A_1)	 τ_2 (A_2)	Delayed fluorescence τ_1 (A_1)	 τ_2 (A_2)	Φ_{Total}
BNO							
Hexane	310	605	13.60 ns (100%)		6.38 μs (100%)		0.12
DMSO–water mixture (f_w = 70%)	310	535	14.58 ns (100%)	—	60.07 μs (6.71%)	146.04 μs (93.29%)	0.25
DMSO–water mixture (f_w = 90%)	310	580	10.39 ns (14.93%)	15.64 ns (85.07%)	24.98 μs (78.17%)	109.49 μs (21.83%)	0.19
BNS							
Hexane	280	620	11.18 ns (100%)				
DMSO–water mixture (f_w = 90%)	280	580	10.31 ns (100%)	—	13.52 μs (66.58%)	32.96 μs (33.42%)	0.32

τ = lifetime, A is the amplitude of intensity, Φ_{Total} is total PLQY, and λ_{ex} and λ_{em} are the excitation and emission wavelengths, respectively.

Solid-state PL studies. As in the solution state, **BNO** in the solid state shows a broad emission band ranging from 450 to 750 nm with a peak maximum at 545 nm, which is found to be 25 nm and 50 nm red-shifted with respect to **BNS** and **R1**, respectively (Fig. 5a). This bathochromic shift can be attributed to the difference in solid-state packing upon changing the donor from PXZ to PTZ of **BNO** and **BNS** and the change in the dixylylboryl acceptor in **BNO** to dimesitylboryl in **R1**.[72] The **BNO** emission bands are insensitive to the excitation, indicating that the emission originates from the lowest excited state irrespective of the initial excitation (Fig. S26a†). The fluorescence lifetime of **BNO** (~13.92 ns) is relatively higher than that of **BNS** (~9.87) and **R1** (10.0 ns) resulting from the high radiative and low non-radiative decay rates of **BNO** compared to those of others (Tables 2 and S11†). Interestingly, the PLQY of **BNO** is very high and is ~ 4 times higher than that of **BNS**. As in the solution and aggregate states, **BNO** also exhibits DF in the solid state as well with a lifetime of 103.65 μs (Fig. 5b). Both PL intensity and lifetimes, increased significantly under vacuum (in the absence of oxygen), confirming the involvement of triplet states (Fig. 5c, d, S27, and Table S11†). Excitation spectra of **BNO** in the solid state are completely different from those of **BNO** in the solution state indicating the difference in the emitting states (Fig. S26b†).

To further validate the nature of DF, the PL studies were conducted at various temperatures under vacuum (Fig. S28

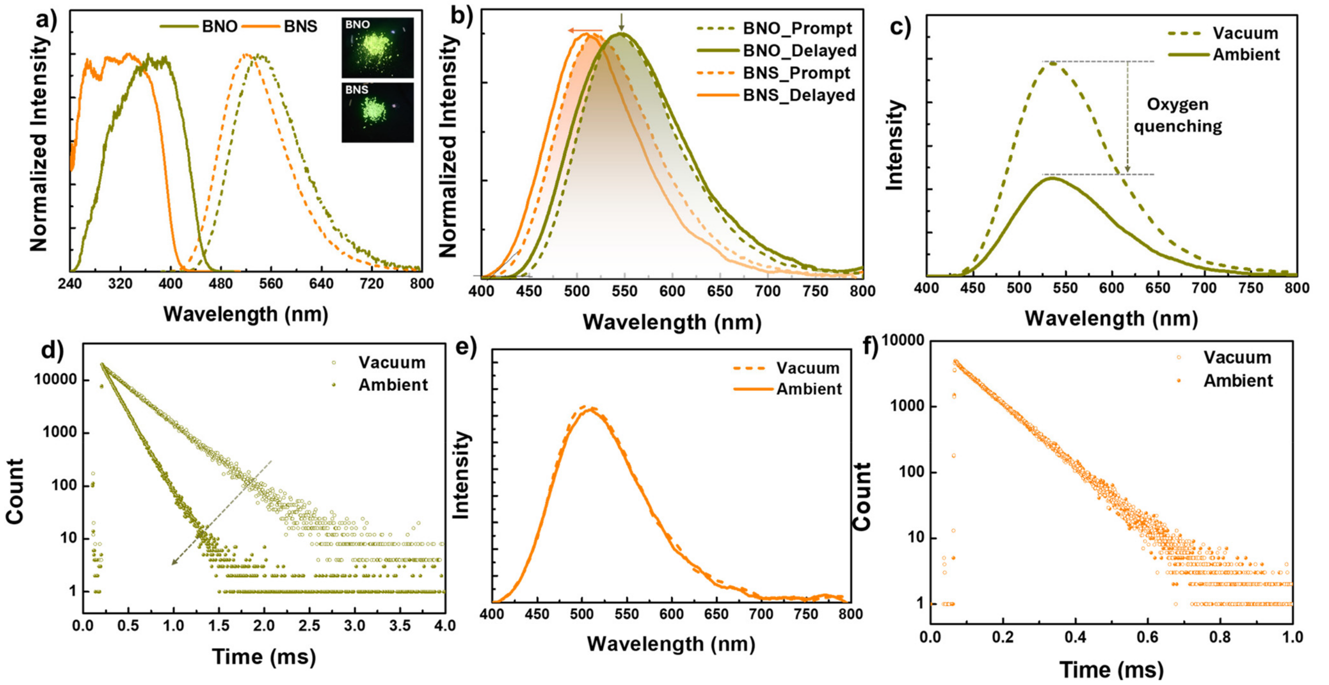

Fig. 5 (a) Steady-state PL (dashed lines) and excitation spectra for the solid samples of **BNO** and **BNS** (λ_{ex} = 375 nm). (b) Prompt and time-gated [50 μs delay] PL spectra for solid samples of **BNO** and **BNS** (λ_{ex} = 375 nm and 350 nm) at 298 K under ambient conditions. (c) Time-gated [50 μs delay] PL spectra and (d) delayed fluorescence decay (λ_{em} = 540 nm) for the solid sample of **BNO**. (e) Time-gated [50 μs delay] PL spectra and (f) phosphorescence decay (λ_{em} = 500 nm) for solid samples of **BNS** under vacuum (absence of oxygen) and ambient (in the presence of oxygen) conditions.

Table 2 Important photophysical parameters (average prompt fluorescence (PF), delayed fluorescence (DF)/phosphorescence (PH)* lifetime, total photoluminescence quantum yield, and radiative and non-radiative decay rate constants) for **BNO** and **BNS** at 298 K under ambient conditions

Compound	$\lambda_{\text{em (Fl)}}$ (nm)	PF lifetime	$\lambda_{\text{em (DF/PH)}}$ (nm)	PH/DF lifetime	Φ_{Total}	k_r $[10^6]$ s^{-1}	k_{nr} $[10^7]$ s^{-1}
BNO (solid)	545	13.92 ns	540	103.65 µs	0.74	54.33	1.91
BNO (Neat film)	545	14.02 ns	545	99.02 µs	0.63	44.93	2.64
BNO (1 wt%@ PMMA)	568	15.92 ns	568	41.63 µs	0.3	19.62	4.57
BNS (solid)	520	9.87 ns	500*	91.03 µs	0.2	20.26	8.10
BNS (Neat film)	500	8.71 ns	535*	73.30 µs	0.6	68.88	4.59
BNS (1 wt%@ PMMA)	575	12.26 ns	550*	69.05 µs	0.41	33.44	4.81

Fl is the fluorescence, τ = average lifetime, Φ_{Total} is the total PLQY, while k_r (=Φ/τ_{Fl}), k_{nr} (=1−Φ/τ_{Fl}), are the radiative decay from S_1, the non-radiative decay from S_1, the λ_{ex}, and λ_{em}, are the excitation wavelength and the emission wavelength, respectively.

and Table S11†). As the temperature is increased, the prompt PL intensity and lifetime increase significantly, indicating the thermally activated delayed fluorescence (TADF) process (Fig. S28a†). In contrast, the DF intensity decreased with increasing temperature, which can be attributed to the temperature-assisted deactivation of triplet states at a higher temperature state (Fig. S28c†). At lower temperatures, this compound showed a longer PL decay time than at higher temperatures (Fig. S28d and Table S11†). At 298 K, rISC predominates over radiative and non-radiative decay from the triplet state, resulting in TADF emission.

Steady-state PL and triboluminescence characteristics of **BNS** were demonstrated by Neena *et al.* in 2017.[64] However, they did not explore the delayed luminescence features of this compound. Hence, we studied the delayed luminescence of this compound in detail and compared the results with those of **BNO**. **BNS** exhibits a broad emission like **BNO** with a peak maximum at 520 nm and lifetime of ∼9.87 ns, which are comparable to the reported data (Fig. 5a and Table 2). The time-gated PL spectrum of **BNS** appeared at ∼510 nm, which is 10 nm blue-shifted compared with the prompt fluorescence (PF) spectrum (Fig. 5a). This band (∼510 nm) exhibited a lifetime of 91.03 µs in contrast to the ns lifetime of PF (Fig. 5f and Table 2). The PL intensity and lifetime of delayed bands are sensitive to oxygen, and thus, this band has been ascribed to phosphorescence (PH) (Fig. 5e, f and S29†).

Furthermore, the PF and PH lifetimes of this compound were recorded at different temperatures (Fig. S30 and Table S11†). The intensity of both PF and PH bands increased steadily as the temperature decreased from 298 to 77 K. Furthermore, the peak maximum of the PH is ∼5 nm red-shifted at 77 K than at 298 K. However, such a spectral shift is absent for PF, indicating that temperature-dependent structural reorganization affects the triplet manifold, not the singlet (Fig. S30a and c†). Furthermore, the lifetime of PF showed marginal changes with respect to temperature; however, the PH lifetime steeply increased from microseconds to hundreds of milliseconds (Fig. S30d and Table S11†). These results indicate that **BNS** shows blue-shifted RTP, a phenomenon very rarely demonstrated in the literature.[87–91] This blue-shifted RTP band can be attributed to PH from a higher energy triplet state (T_n), which is at slightly higher energy than S_1 and has a significantly larger energy gap from the T_1 state. Moreover, the inherent conformation-switching properties of phenothiazine between quasi-axial and quasi-equatorial at the excited state can also result in re-organizing electronic states. This hypothesis is well-supported by the computational studies (*vide infra*) detailed in the last sub-section.[68–75]

PL studies in thin film. After successfully demonstrating the delayed emission features in the solid state, we investigated the photoluminescent properties of **BNO** and **BNS** in thin films. These compounds were doped into a PMMA matrix at various loading concentrations (1 wt%, 10 wt%, and 50 wt%), and PL spectra were recorded, and the results were compared with those of neat films (Fig. 6, S31–S40 and Tables S12–S15†). This approach enabled us to demonstrate how intermolecular interactions affect the PL properties moving from a molecularly dispersed state (1 wt% in PMMA) to an aggregated state (neat film).

The PF maxima of films doped with (1, 10, and 50 wt%) **BNO** (λ_{em} = 568 nm) and **BNS** (λ_{em} = 575 nm) show a bathochromic shift compared to their respective solids (Fig. 6a and d). However, the spectral shift is more significant in **BNS** (55 nm) than in **BNO** (23 nm). The PF band intensity in **BNO** increased when the doping concentration increased from 1 wt% to 10 wt%, while the PL intensity decreased for 50 wt% doping. In contrast, for **BNS**, the PL intensity gradually increased when increasing the doping concentration from 1 wt% to 50 wt% (Fig. 6a and d). The PF of neat films of both compounds show a hypsochromic shift (545 nm for **BNO** and 500 nm for **BNS**) compared to their doped films; however, **BNS** showed a stronger blue shift (75 nm) than **BNO** (23 nm) (Fig. 6b and e). Interestingly, the neat film of **BNO** showed brighter luminescence than doped films (Φ_{Total} = 0.3, 0.48, 0.5, and 0.63 for 1 wt%, 10 wt%, 50 wt%, and neat, respectively). On the other hand, the neat film of **BNS** was less luminescent (Φ_{Total} = 0.60) than 50 wt% (Φ_{Total} = 0.87) doped film and higher than 10 wt% (Φ_{Total} = 0.54) and 1 wt% doped film (Φ_{Total} = 0.41). Furthermore, the PF of the neat film of **BNO** matched exactly with the PF of the solid (545 nm). In contrast, the **BNS** (500 nm) showed a 20 nm blue shift compared to its solid PF (520 nm). The PF lifetime of these compounds falls within the ns region confirming the fluorescence nature of these bands. Moreover, the PF lifetime values follow the same trend observed for their respective PF intensity values (Tables S12 and S14†).

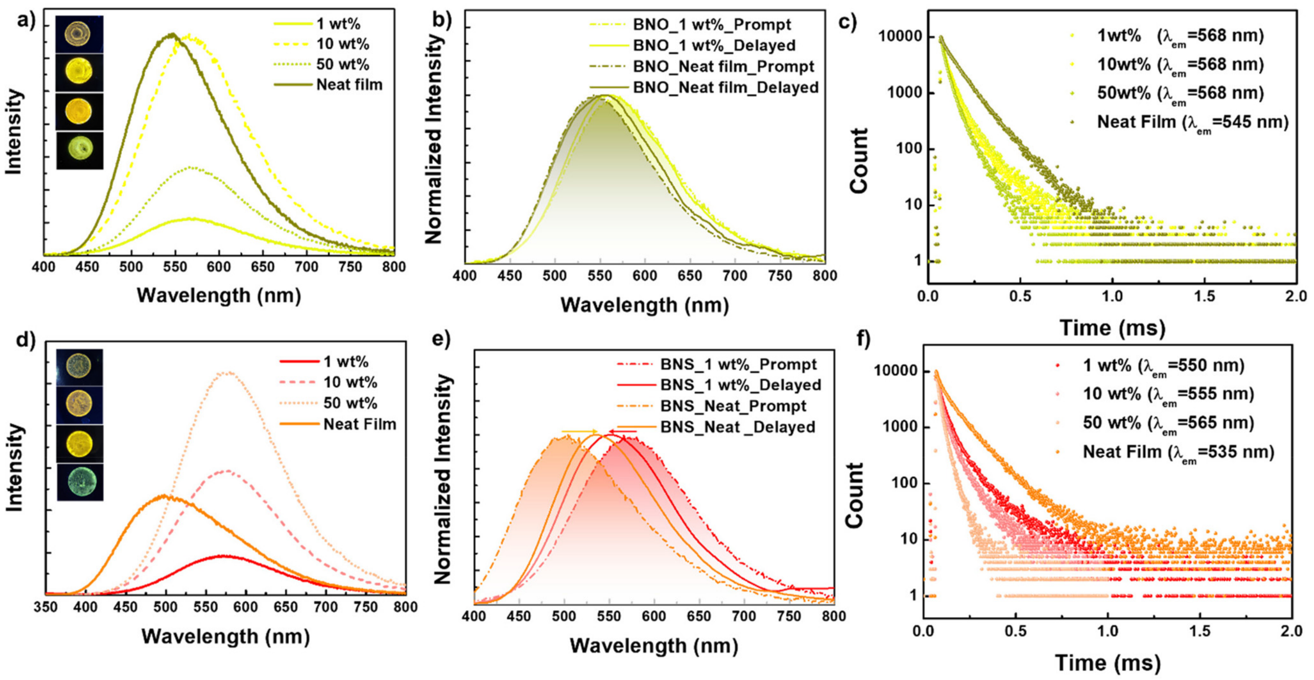

Fig. 6 Steady-state PL spectra for (a) **BNO** and (d) **BNS** doped into PMMA at different doping concentrations and neat film at λ_{ex} = 330 nm under vacuum (in the absence of oxygen). Prompt and time-gated/delayed [30 μs delay] PL spectra of (b) **BNO** and (e) **BNS** doped into PMMA (1wt%) and neat film at λ_{ex} = 330 nm under vacuum (in the absence of oxygen). (c) Delayed fluorescence decay for **BNO** doped into PMMA at different doping concentrations and neat film at λ_{ex} = 330 nm under vacuum (in the absence of oxygen). (f) Phosphorescence decay for **BNS** doped into PMMA at different doping concentrations and neat film at λ_{ex} = 330 nm under vacuum (in the absence of oxygen).

The DF intensity of doped (1, 10, and 50 wt%) and neat films of **BNO**, exhibited a similar trend that was observed for PF intensities. In contrast, the doped films (1, 10, and 50 wt%) of **BNS** show blue-shifted PH, and the peak intensity follows the same trend as that observed for PF (Fig. 6b and e). The extent of the hypsochromic spectral shift is susceptible to the doping concentrations; the maximum spectral shift was observed for 1 wt% doping (25 nm). Interestingly, the PH of the neat film of **BNS** (535 nm) shows a bathochromic shift compared to its PF (500 nm) and PH of crystals (500 nm). The DF and PH of neat and doped films of **BNO** and **BNS** exhibit PL lifetimes in the μs range; furthermore, these lifetimes decrease upon increasing the doping concentration (Fig. 6c and f). The PL lifetime of the neat film of both compounds was higher than that of doped films and lower than their respective solids.

The PF and DF (**BNO**) or PH (**BNS**) of these compounds were recorded at different temperatures, under ambient (in the presence of O_2) and vacuum (in the absence of O_2) conditions at RT (298 K) (Fig. S33–S35 and S38–40†). The PL intensity of **BNO** and **BNS** are sensitive to oxygen and showed stronger luminescence under vacuum. The PF and DF peak intensity of both **BNO** and **BNS** increased as the temperature decreased from 298 K to 77 K. However, in both cases, the change in peak intensity is more pronounced for DF/PH compared to their respective PF intensity.

The PH band of thin films (doped and neat films) of **BNS** shows a blue shift as the temperature decreases from 298 to 77 K. Unlike in the crystalline state, the PF of neat films of **BNS** also shows a hypsochromic shift at low temperatures. Such spectral shifts are not observed in thin films of **BNO**. The temperature-dependent PF and PH of **BNS** can be attributed to the temperature-dependent preferential stabilization of its conformer. Moreover, the unprecedented shift in the PF and PH band in **BNS** upon changing the doping concentration from 1 wt% to neat can be attributed to perturbations in the dynamics between different molecular conformers (quasi-axial and quasi-equatorial), which alter the energy of the singlet and triplet manifold.[68–75] The PL lifetimes recorded for **BNO** and **BNS** at different temperatures show that both the PF and DF or PH are progressively increased upon lowering the temperature (Fig. S33f, S35f, S38f, and S40f†). However, the quantum of increment is considerably higher for the DF and PH than it is for their PF, which can be attributed to the blocking of non-radiative decay of triplet manifolds at lower temperatures. Furthermore, the DF in **BNO** and PH in **BNS** clearly suggest that the stabilization of the triplet manifold and the rate of the rISC process highly depend on the heteroatom attached to the cyclic amine donor.[53–55,92] This conclusion is further augmented by computational results discussed *vide-infra*.

Excited state theoretical studies. To further understand the emission characteristics in-depth, we investigated the electronic states of these compounds through DFT and TD-DFT studies. Both **BNO** and **BNS** exist in a quasi-axial conformation at the ground state, with dipole moments of 0.82 D and 1.29 D for **BNO** and **BNS**, respectively. Upon photoexcitation, the PXZ and PTZ units in **BNO** and **BNS** become more planar, adopting a quasi-equatorial conformation in their S_1 and T_1 states (Fig. 7a, b and S41, S42†). However, in the T_1 state, the BN bond lengths, PTZ or PXZ puckering angles, and dipole moments have changed significantly compared to those in the S_1 state (Table S16†). Furthermore, the frontier molecular orbitals (FMOs) of these S_1 states are localized on distinct regions of the molecule, indicating a charge-transfer (CT) character of the state, consequently resulting in higher dipole moments (6.56 D for **BNO** and 3.43 D for **BNS**) (Fig. S41, S42 and Table S16†).

The energy levels of **BNO** and **BNS**, derived from singlet and triplet vertical transition calculations, are illustrated in Fig. 7a and b (Fig. S45 and Tables S18, S19†). It is quite evident from the diagram that the ΔE_{S1-T1} in **BNO** (0.67 eV) and **BNS** (0.70 eV) is relatively large, making efficient intersystem crossing (ISC) challenging. However, higher triplet states (T_n), specifically T_5 for **BNO** and T_6 for **BNS**, are energetically closer to S_1 ($\Delta E_{S1-Tn} < 150$ meV), making them favorable for efficient ISC. The experimental ΔE_{ST} value determined from the spectral onset values further supports the claim (Table S17; see the ESI† for more details).

For **BNO**, T_5 is energetically closer to S_1 ($\Delta E_{S1-T5} = 140$ meV) and exhibits a significant spin–orbit coupling constant (ξ_{SOC}) of 0.1910 cm^{-1}. The substantial energy difference between T_5 and T_4 favors efficient reverse intersystem crossing (rISC) rather than radiative or non-radiative decay from T_5 and drives delayed fluorescence at room temperature (Fig. 7a, S45a and Table S18†). Moreover, the natural transition orbital (NTO) analysis shows that T_5 has a pronounced locally excited (LE) character, whereas S_1 has a pure charge-transfer (CT) character. This difference in symmetry further promotes ISC and rISC (El-Sayed's rule) (Fig. 7c and S43†).[56,57]

In **BNS**, T_5 and T_6 are energetically close to S_1 through which efficient spin crossover is possible. Among these two states, T_6 is slightly higher in energy than S_1 ($\Delta E_{S1-T6} = 10$ meV) but has a considerably higher ξ_{SOC} (0.7679 cm^{-1}) than T_5 (0.4358 cm^{-1}), and is about four times higher than that of **BNO**, leading to efficient ISC to T_6 (Fig. 7b, S45b and Table S18†). This large difference in SOC can be attributed to the heavy atom effect of S over O. Additionally, the large energy gap between T_5 and T_4 reduces the chances of non-

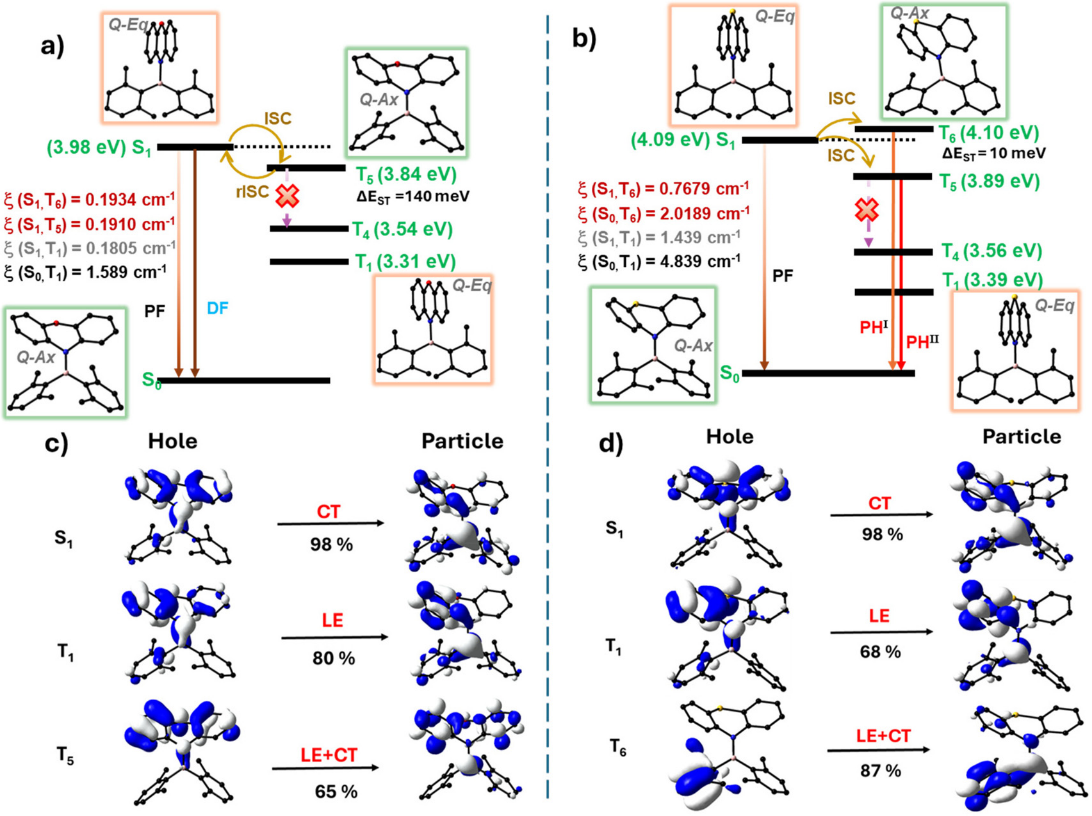

Fig. 7 Energy level diagrams showing plausible singlet to triplet transitions (ISC/rISC), the singlet–triplet energy gap, spin–orbit coupling constant (ξ_{SOC}), and geometry of the corresponding electronic states for (a) **BNO** and (b) **BNS**. FL = fluorescence, DF = delayed fluorescence, PH^{I} = blue-shifted phosphorescence (doped film and solid), and PH^{II} = red-shifted phosphorescence (neat film). Energy levels in the diagram are not to scale and obtained from the vertical transition calculations using TD-DFT and the B3LYP/6-31G(d) level of theory. Geometry optimization is done using DFT/TD-DFT at the same level of theory by taking coordinates from crystal data and after single-point energy calculations. Natural transition orbitals for (c) **BNO** and (d) **BNS** at the S_1, T_5, and T_6 states.

radiative decay, confining competing processes to rISC ($T_6 \rightarrow S_1$) and radiative decay from $T_6 \rightarrow S_0$ or $T_5 \rightarrow S_0$. The ξ_{SOC} calculated for S_0–T_6 is nearly three times higher than that of S_1–T_6, resulting in a high-energy (blue-shifted) phosphorescence (PH^I), especially in a rigid isolated environment. While in the neat film, non-radiative deactivation of the $T_6 \rightarrow T_5$ state occurred due to molecular collision at high compound concentration, followed by emission from T_5 (red-shifted phosphoresce – PH^{II}) (Fig. 7b and S45b†). In addition, **BNS** in T_5 and T_6 adopted a quasi-axial conformation with a prominent LE character, which is different from the S_1 geometry (quasi-equatorial with pure CT character) further facilitating ISC and phosphorescence (Fig. 7d and S44†).

In short, the large energy gap between the S_1 and the T_1 states in **BNO** and **BNS** results in the spin crossover (ISC and rISC) occurring *via* the energetically favorable T_5 or T_6 states. In **BNO**, efficient rISC occurs under favorable energy conditions at room temperature, leading to TADF. In contrast, for **BNS**, due to the large energy gap between T_6 or T_5 and T_4 combined with the higher SOC between S_0 and T_6, a radiative emission from T_6 is favored, producing blue-shifted phosphorescence in isolated rigid environments (solid and doped films). Additionally, the involvement of different conformations in excited states (especially in **BNS**) causes these states to vary their energetics with respect to the microenvironment and molecular interactions.[68–75] This sensitivity may explain the anomalous shift in the phosphorescence band observed in thin films as the doping concentration increases from 1 wt% to 100 wt%, leading to unprecedented phosphorescent behaviour.

Conclusion

In conclusion, we investigated the delayed luminescence properties of aminoboranes **BNO** and **BNS** with phenoxazine (PXZ) or phenothiazine (PTZ) donors and dixylylborane acceptors. **BNO** and **BNS** exhibit broad emission in solution (450–800 nm) with large Stokes shifts and low PLQYs due to the excited state conformational changes of nonplanar cyclic amine donors. **BNO** shows TADF in the solution state; however, **BNS** does not show TADF, which can be attributed to the combined heavy atom (S) and the extensive flip-flop motion of phenothiazine-mediated non-radiative triplet deactivation in dilute solutions. Both the compounds exhibit AIEE and DF in aggregates due to the restriction of intramolecular motion. The aggregates of **BNO** demonstrate tunable emission from greenish-yellow to orange-red and efficient TADF in solid and thin films. In contrast, **BNS** shows rare, blue-shifted phosphorescence in solid and doped films. The extent of this blue shift in phosphorescence compared to the prompt fluorescence depends on the doping concentration, confirming the role of intermolecular interactions in stabilizing the triplet state. On the other hand, neat films of **BNS** exhibit PTZ-centered, red-shifted phosphorescence. Excited-state computational studies reveal that these compounds undergo significant conformational changes, alternating between quasi-axial and quasi-equatorial forms. These dynamic conformations perturb the energetics of triplet and singlet states, particularly in **BNS**, which leads to unusual phosphorescence shifts. Additionally, ISC and rISC were found to occur *via* higher triplet states (T_5 or T_6) in both compounds. In **BNO**, low ΔE_{S1-T5} favors rISC for efficient TADF emission. In **BNS**, the substantial energy gap between T_6 or T_5 and T_4, combined with strong spin–orbit coupling between T_6 and S_0, results in unique, blue-shifted phosphorescence, which has not been observed for aminoboranes.

Data availability

Details on the synthesis and structural characterization, photophysical and DFT and TD-DFT results are available in the ESI, and Crystallographic data available in CCDC (CCDC 2402292 for **BNO**).

The data supporting this article have been included as part of the ESI.†

Conflicts of interest

There are no conflicts to declare.

Acknowledgements

The authors thank IISc, SERB for the financial support and Prof K.R. Prasad, Department of Organic Chemistry for the HRMS facility. M. M. A. T. thanks CSIR India for the research fellowship. S. J. thanks IISc for the research fellowship.

References

1 Y. Yang, F. Gao, Y. Wang, H. Li, J. Zhang, Z. Sun and Y. Jiang, *Molecules*, 2022, **27**, 8421.

2 H.-Z. Li, F.-M. Xie, Y.-Q. Li and J.-X. Tang, *J. Mater. Chem. C*, 2023, **11**, 6471–6511.

3 Kenry, C. Chen and B. Liu, *Nat. Commun.*, 2019, **10**, 2111.

4 W. Zhao, Z. He and B. Z. Tang, *Nat. Rev. Mater.*, 2020, **5**, 869–885.

5 K. R. Naveen, H. I. Yang and J. H. Kwon, *Commun. Chem.*, 2022, **5**, 149.

6 Y.-Z. Shi, H. Wu, K. Wang, J. Yu, X.-M. Ou and X.-H. Zhang, *Chem. Sci.*, 2022, **13**, 3625–3651.

7 M. Y. Wong and E. Zysman-Colman, *Adv. Mater.*, 2017, **29**, 160544.

8 Y. Im, M. Kim, Y. J. Cho, J.-A. Seo, K. S. Yook and J. Y. Lee, *Chem. Mater.*, 2017, **29**, 1946–1963.

9 T. Zhang, Y. Xiao, H. Wang, S. Kong, R. Huang, V. Ka-Man Au, T. Yu and W. Huang, *Angew. Chem., Int. Ed.*, 2023, **62**, e202301896.

10 H. E. Hackney and D. F. Perepichka, *Aggregate*, 2022, **3**, e123.

11 A. D. Nidhankar, Goudappagouda, V. C. Wakchaure and S. S. Babu, *Chem. Sci.*, 2021, **12**, 4216–4236.

12 Z. Y. Liu, J. W. Hu, C. H. Huang, T. H. Huang, D. G. Chen, S. Y. Ho, K. Y. Chen, E. Y. Li and P. T. Chou, *J. Am. Chem. Soc.*, 2019, **141**, 9885–9894.

13 Y. Tao, C. Liu, Y. Xiang, Z. Wang, X. Xue, P. Li, H. Li, G. Xie, W. Huang and R. Chen, *J. Am. Chem. Soc.*, 2022, **144**, 6946–6953.

14 R. Wang, Y. Zhu, Z. Xia, K. Liang, L. Kong, J. Liu, W. Shi and C. Lu, *J. Mater. Chem. C*, 2022, **10**, 17182–17189.

15 Z. Wu, J. Nitsch, J. Schuster, A. Friedrich, K. Edkins, M. Loebnitz, F. Dinkelbach, V. Stepanenko, F. Würthner, C. M. Marian, L. Ji and T. B. Marder, *Angew. Chem., Int. Ed.*, 2020, **59**, 17137–17144.

16 Y. Huo, J. Lv, Y. Xie, L. Hua, Y. Liu, Z. Ren, T. Li, S. Ying and S. Yan, *ACS Appl. Mater. Interfaces*, 2022, **14**, 57092–57101.

17 U. P. Pandey, R. P. Nandi and P. Thilagar, *Front. Chem.*, 2020, **8**, 541331.

18 U. P. Pandey and P. Thilagar, *Adv. Opt. Mater.*, 2020, **8**, 1902145.

19 S. Pagidi, N. K. Kalluvettukuzhy and P. Thilagar, *Inorg. Chem.*, 2020, **59**, 3142–3151.

20 S. Jena, P. Dhanalakshmi, G. Bano and P. Thilagar, *J. Phys. Chem. B*, 2020, **124**, 5393–5406.

21 S. K. Sarkar, M. Pegu, S. K. Behera, S. K. Narra and P. Thilagar, *Chem. – Asian J.*, 2019, **14**, 4588–4593.

22 K. K. Neena, P. Sudhakar and P. Thilagar, *Angew. Chem.*, 2018, **130**, 17048–17052.

23 S. R. Pristash, K. L. Corp, E. J. Rabe and C. W. Schlenker, *ACS Appl. Energy Mater.*, 2020, **3**, 19–28.

24 T. Serevičius, R. Komskis, P. Adomėnas, O. Adomėnienė, G. Kreiza, V. Jankauskas, K. Kazlauskas, A. Miasojedovas, V. Jankus, A. Monkman and S. Juršėnas, *J. Phys. Chem. C*, 2017, **121**, 8515–8524.

25 S. M. Suresh, E. Duda, D. Hall, Z. Yao, S. Bagnich, A. M. Z. Slawin, H. Bässler, D. Beljonne, M. Buck, Y. Olivier, A. Köhler and E. Zysman-Colman, *J. Am. Chem. Soc.*, 2020, **142**, 6588–6599.

26 D. Hertel, H. Bässler, R. Guentner and U. Schert, *J. Chem. Phys.*, 2001, **115**, 10007–10013.

27 S. Oda, W. Kumano, T. Hama, R. Kawasumi, K. Yoshiura and T. Hatakeyama, *Angew. Chem., Int. Ed.*, 2021, **60**, 2882–2886.

28 Y. Kondo, K. Yoshiura, S. Kitera, H. Nishi, S. Oda, H. Gotoh, Y. Sasada, M. Yanai and T. Hatakeyama, *Nat. Photonics*, 2019, **10**, 678–668.

29 G. Méhes, H. Nomura, Q. Zhang, T. Nakagawa and C. Adachi, *Angew. Chem., Int. Ed.*, 2012, **51**, 11311–11315.

30 D. G. Congrave, B. H. Drummond, P. J. Conaghan, H. Francis, S. T. E. Jones, C. P. Grey, N. C. Greenham, D. Credgington and H. Bronstein, *J. Am. Chem. Soc.*, 2019, **141**, 18390–18394.

31 H. Uoyama, K. Goushi, K. Shizu, H. Nomura and C. Adachi, *Nature*, 2012, **492**, 234–238.

32 W. Chi, J. Chen, W. Liu, C. Wang, Q. Qi, Q. Qiao, T. M. Tan, K. Xiong, X. Liu, K. Kang, Y. T. Chang, Z. Xu and X. Liu, *J. Am. Chem. Soc.*, 2020, **142**, 6777–6785.

33 Y. Pan, W. Li, S. Zhang, L. Yao, C. Gu, H. Xu, B. Yang and Y. Ma, *Adv. Opt. Mater.*, 2014, **2**, 510–515.

34 W. Li, Y. Pan, R. Xiao, Q. Peng, S. Zhang, D. Ma, F. Li, F. Shen, Y. Wang, B. Yang and Y. Ma, *Adv. Funct. Mater.*, 2014, **24**, 1609–1614.

35 S. Zhang, W. Li, L. Yao, Y. Pan, F. Shen, R. Xiao, B. Yang and Y. Ma, *Chem. Commun.*, 2013, **49**, 11302–11304.

36 W. Li, D. Liu, F. Shen, D. Ma, Z. Wang, T. Feng, Y. Xu, B. Yang and Y. Ma, *Adv. Funct. Mater.*, 2012, **22**, 2797–2803.

37 K. Goushi, K. Yoshida, K. Sato and C. Adachi, *Nat. Photonics*, 2012, **6**, 253–258.

38 D. G. Chen, T. C. Lin, C. L. Chen, Y. T. Chen, Y. A. Chen, G. H. Lee, P. T. Chou, C. W. Liao, P. C. Chiu, C. H. Chang, Y. J. Lien and Y. Chi, *ACS Appl. Mater. Interfaces*, 2018, **10**, 12886–12896.

39 Y. J. Lien, T. C. Lin, C. C. Yang, Y. C. Chiang, C. H. Chang, S. H. Liu, Y. T. Chen, G. H. Lee, P. T. Chou, C. W. Lu and Y. Chi, *ACS Appl. Mater. Interfaces*, 2017, **9**, 27090–27101.

40 P. Ganesan, D. G. Chen, W. C. Chen, P. Gnanasekaran, J. A. Lin, C. Y. Huang, M. C. Chen, C. S. Lee, P. T. Chou and Y. Chi, *J. Mater. Chem. C*, 2020, **8**, 4780–4788.

41 J. Zhi, Q. Zhou, H. Shi, Z. An and W. Huang, *Chem. – Asian J.*, 2020, **15**, 947–957.

42 F. Fang, L. Zhu, M. Li, Y. Song, M. Sun, D. Zhao and J. Zhang, *Adv. Sci.*, 2021, **8**(24), 2102970.

43 J. R. Caine, P. Hu, A. T. Gogoulis and Z. M. Hudson, *Acc. Mater. Res.*, 2023, **4**, 879–891.

44 J. You, X. Zhang, Q. Nan, K. Jin, J. Zhang, Y. Wang, C. Yin, Z. Yang and J. Zhang, *Nat. Commun.*, 2023, **14**, 4163.

45 Y. Li and P. Gao, *Chemosensors*, 2023, **11**, 489.

46 R. Arumugam, A. T. M. Munthasir, R. Kannan, D. Banerjee, P. Sudhakar, V. R. Soma, P. Thilagar and V. Chandrasekhar, *Chem. Sci.*, 2024, **15**, 18364–18378.

47 M. Ji and X. Ma, *Ind. Chem. Mater.*, 2023, **1**, 582–594.

48 D. Li, J. Guo, L. Zhao, G. Zhang and G. Yan, *RSC Adv.*, 2019, **9**, 31953–31959.

49 C. J. Christopherson, D. M. Mayder, J. Poisson, N. R. Paisley, C. M. Tonge and Z. M. Hudson, *ACS Appl. Mater. Interfaces*, 2020, **12**, 20000–20011.

50 F.-Y. Meng, I.-H. Chen, J.-Y. Shen, K.-H. Chang, T.-C. Chou, Y.-A. Chen, Y.-T. Chen, C.-L. Chen and P.-T. Chou, *Nat. Commun.*, 2022, **13**, 797.

51 X. Chen, J. Zhang, C. Liu, Q. Lou, K. Zheng, X. Yin, L. Xie, P. Wen, C. Liu and Z. Ge, *ACS Appl. Energy Mater.*, 2021, **4**, 11112–11120.

52 Y. Meng, J. Zhang, C. Liu, K. Zheng, L. Xie, S. Bu, B. Han, R. Cao, X. Yin, C. Liu and Z. Ge, *Adv. Funct. Mater.*, 2023, **33**, 2210600.

53 D. R. Lee, K. H. Lee, W. Shao, C. L. Kim, J. Kim and J. Y. Lee, *Chem. Mater.*, 2020, **32**, 2583–2592.

54 U. Balijapalli, M. Tanaka, M. Auffray, C. Y. Chan, Y. T. Lee, Y. Tsuchiya, H. Nakanotani and C. Adachi, *ACS Appl. Mater. Interfaces*, 2020, **12**, 9498–9506.

55 S. Jena, S. K. Behera, J. Eyyathiyil, M. Kitahara, Y. Imai and P. Thilagar, *Adv. Opt. Mater.*, 2023, **11**, 2300923.

56 M. A. El-Sayed, *J. Chem. Phys.*, 1963, **38**, 2834–2838.
57 M. Baba, *J. Phys. Chem. A*, 2011, **115**, 9514–9519.
58 J. Eng and T. J. Penfold, *Chem. Rec.*, 2020, **20**, 831–856.
59 N. Aizawa, Y. Harabuchi, S. Maeda and Y. J. Pu, *Nat. Commun.*, 2020, **1**, 3909.
60 L. Ji, S. Griesbeck and T. B. Marder, *Chem. Sci.*, 2017, **8**, 846–863.
61 L. Xu, K. Zhou, X. Qiu, B. Rao, D. Pei, A. Li, Z. An and G. He, *J. Mater. Chem. C*, 2020, **8**, 14740–14747.
62 R. P. Nandi, N. K. Kalluvettukuzhy, S. Pagidi and P. Thilagar, *Inorg. Chem.*, 2023, **62**, 1122–1134.
63 K. K. Neena, P. Sudhakar and P. Thilagar, *Angew. Chem.*, 2018, **130**, 17048–17052.
64 K. K. Neena, P. Sudhakar, K. Dipak and P. Thilagar, *Chem. Commun.*, 2017, **53**, 3641–3644.
65 P. Sudhakar, K. K. Neena and P. Thilagar, *J. Mater. Chem. C*, 2017, **5**, 6537–6546.
66 N. K. Kalluvettukuzhy, P. Sudhakar, J. Eyyathiyil, N. Hara, Y. Imai and P. Thilagar, *Org. Lett.*, 2023, **25**, 6067–6071.
67 K. K. Neena and P. Thilagar, *J. Mater. Chem. C*, 2016, **4**, 11465–11473.
68 R.-N. Su, Q.-Q. Pan, G.-Y. Ding, J. Sun, L.-L. Wen, K.-Z. Shao, S.-B. Wang, G.-G. Shan and Z.-M. Su, *J. Mater. Chem. C*, 2023, **11**, 9908–9915.
69 Y. Tian, J. Yang, A. Li, J. Ren, X. Li, M. Fang and Z. Li, *ACS Mater. Lett.*, 2024, **6**, 943–953.
70 Q. Zhou, C. Yang and Y. Zhao, *Chem*, 2023, **9**, 2446–2480.
71 F. Khan and R. Misra, *J. Mater. Chem. C*, 2023, **11**, 2786–2825.
72 M. Gao, Y. Tian, X. Li, Y. Gong, M. Fang, J. Yang and Z. Li, *Angew. Chem., Int. Ed.*, 2023, **5**, e202214908.
73 M. Gao, Y. Tian, J. Yang, X. Li, M. Fang and Z. Li, *J. Mater. Chem. C*, 2021, **9**, 15375–15380.
74 Y. Wang, J. Yang, M. Fang, Y. Gong, J. Ren, L. Tu, B. Z. Tang and Z. Li, *Adv. Funct. Mater.*, 2021, **40**, 2101719.
75 T. Song, H. Liu, J. Ren and Z. Wang, *Adv. Opt. Mater.*, 2024, **1**, 2301215.
76 C. A. Swami and P. Thilagar, *Inorg. Chem.*, 2014, **53**, 2776–2786.
77 S. K. Sarkar, S. E. Rao and P. Thilagar, *J. Phys. Chem. B*, 2020, **124**, 8896–8903.
78 P. Thilagar, R. P. Nandi and S. Ghosh, *Chem. – Eur. J.*, 2024, **30**, e202400398.
79 S. Pagidi, N. K. Kalluvettukuzhy and P. Thilagar, *Organometallics*, 2018, **37**, 1900–1909.
80 N. J. Hestand and F. C. Spano, *Chem. Rev.*, 2018, **118**, 7069–7163.
81 R. Hu, E. Lager, A. Aguilar-Aguilar, J. Liu, J. W. Y. Lam, H. H. Y. Sung, I. D. Williams, Y. Zhong, K. S. Wong, E. Peña-Cabrera and B. Z. Tang, *J. Phys. Chem. C*, 2009, **113**, 15845–15853.
82 X. Lu, Y. Hu, H. Liu, J. Qi, X. Chen, Y. Sun and W. Hu, *Adv. Opt. Mater.*, 2022, **20**, 2201075.
83 J. Xu, X. Zhu, J. Guo, J. Fan, J. Zeng, S. Chen, Z. Zhao and B. Z. Tang, *ACS Mater. Lett.*, 2019, **1**, 613–619.
84 N. Aizawa, C.-J. Tsou, I. S. Park and T. Yasuda, *Polym. J.*, 2017, **49**, 197–202.
85 D. Barman and P. K. Iyer, *J. Phys. Chem. C*, 2023, **127**, 2694–2704.
86 B. Zhang, Y. Kong, H. Liu, B. Chen, B. Zhao, Y. Luo, L. Chen, Y. Zhang, D. Han, Z. Zhao, B. Z. Tang and L. Niu, *Chem. Sci.*, 2021, **12**, 13283–13291.
87 K. Veys and D. Escudero, *Acc. Chem. Res.*, 2022, **55**, 2698–2707.
88 W. Xie, W. Huang, J. Li, Z. He, G. Huang, B. S. Li and B. Z. Tang, *Nat. Commun.*, 2023, **14**, 8098.
89 S. Gao, J. Ding, S. Yu and F. Li, *J. Mater. Chem. C*, 2023, **11**, 6400–6406.
90 Z. Zhu, Z. Kuang, L. Shen, S. Wang, X. Ai, A. Abdurahman and Q. Peng, *Angew. Chem., Int. Ed.*, 2024, e202410552.
91 B. H. Jhun, D. Y. Jeong, S. Nah, S. Y. Park and Y. You, *J. Phys. Chem. C*, 2021, **9**, 7083–7093.
92 S. Jena, J. Eyyathiyil, S. K. Behera, M. Kitahara, Y. Imai and P. Thilagar, *Chem. Sci.*, 2022, **13**, 5893–5901.